Time-resolved entropy measurements using a fast response entropy probe

Meas. Sci. Technol. **19** (2008) 115401 (14pp) doi:10.1088/0957-0233/19/11/115401

Time-resolved entropy measurements using a fast response entropy probe

Michel Mansour[1], **Ndaona Chokani**[1], **Anestis I Kalfas**[2] **and Reza S Abhari**[1]

[1] Laboratory for Energy Conversion, Department of Mechanical and Process Engineering, ETH Zurich, Zurich, Switzerland
[2] Department of Mechanical Engineering, Aristotle University of Thessaloniki, Greece

Received 12 November 2007, in final form 1 July 2008
Published 17 September 2008
Online at stacks.iop.org/MST/19/115401

Abstract
This paper describes a recently developed miniature fast response entropy probe and its application in the turbomachinery facilities at ETH Zurich. The development of the probe is motivated by the need to more clearly document the loss generation mechanisms in the harsh environment of turbomachines. The probe is comprised of a piezoresistive sensor and a pair of thin-film gauges that measure the unsteady pressure and temperature, respectively. The unsteady relative entropy can thus be determined. The design, manufacture and calibration of the probe are first presented in detail. Its application to detail the unsteady entropy field, and associated losses, in a centrifugal compressor, axial turbine and film cooling flows are then described.

Keywords: unsteady flow, heat transfer, entropy measurement

(Some figures in this article are in colour only in the electronic version)

Nomenclature

a	thermal diffusivity
b	axial diffuser width
BR	blowing ratio $= \rho_c U_c / \rho_f U_f$
c_p	specific heat
D	hole diameter
DR	density ratio $= \rho_c / \rho_f$
h	convective heat transfer coefficient, enthalpy
I	feeding current
k	conductivity of the substrate
l	thin-film length
Ma	Mach number
Mu	tip Mach number
Nu	Nusselt number
p	pressure
PSD	power spectral density
q	surface heat transfer
r	thin-film electrical resistivity, recovery factor
R	gas constant, thin-film resistance
R_d	radial measurement position on an impeller
R_{d2}	diameter of an impeller
Re	Reynolds number
s	entropy, Laplace variable (equation (15))
t	thin-film thickness, time
T	temperature
TCR	temperature coefficient of resistance
U	output voltage from a silicon chip
v	velocity
V	voltage
w	thin-film width
x	distance (figure 3), cross-stream direction (figures 19 and 20), thermal penetration depth (equation (13))
X	axial (streamwise) coordinate
Y	stagnation pressure loss coefficient $= \Delta P_0 / \left(0.5 \rho v_{ref}^2\right)$, lateral coordinate
Z	axial position, vertical coordinate

Greek

α_R	temperature coefficient of resistance (linear term)
β_R	temperature coefficient of resistance (quadratic term)
γ	pitch angle, specific heat ratio
η	efficiency
φ	yaw angle
ω	angular frequency

θ normalized total temperature $= \frac{T_T^f - T_T(t)}{T_T^f - T_T^c}$
ρ density
ζ entropy loss coefficient

Superscripts

$''$ per unit of area

Subscripts

2	impeller outlet
aw	adiabatic wall
c	coolant
e	excitation
i	node number
f	freestream
f1, f2	thin films 1, 2
per	jet pulsation period
r	recovery
ref	reference condition
s	static
t	total
gen	generation
cond	conduction
conv	convection

1. Introduction

The primary goal in the design and performance of turbomachines is to have higher efficiencies and wider operating ranges. Thus, a substantial effort has been made to understand the loss mechanisms and their origins in the various components of turbomachines. Although much progress has been made in understanding these loss production mechanisms [1], our understanding is still incomplete. A rational measure of loss can be provided from the standpoint of entropy generation, as has been proposed by Denton [1]. The difficulty, however, is that entropy cannot be measured directly, but only inferred from other measured properties:

$$\Delta s = c_p \ln \frac{T_t}{T_{t,ref}} - R \ln \frac{p_t}{p_{t,ref}}. \quad (1)$$

An advantage of using entropy to rationalize the loss generation is that it is independent of the frame of measurement and it can be readily converted to the practically relevant parameter of efficiency. Nevertheless, the difficulty of simultaneously measuring both unsteady temperature and pressure with both high frequency and spatial resolutions has limited progress in the experimental quantification of the time-resolved loss in turbomachines.

Until now, there have only been a few attempts to simultaneously measure time-resolved temperature and pressure. The aspirating probe was originally designed by Ng and Epstein [2] and was more recently applied by Payne *et al* [3]. The probe is comprised of two hot wires that are placed upstream of a choked orifice. When the two wires are operated at two disparate temperatures, both total pressure and total temperature can be determined. The probe diameter of both Ng and Epstein [2] and Payne *et al* [3] is 3 mm, and the respective measurement bandwidths are 20 kHz and 40 kHz. Passaro *et al* [4] have developed a high-frequency probe to characterize the unsteady pressure and temperature fluctuations in the outflow of a combustor in a gas turbine. The probe consists of a pressure probe, equipped with a Kulite transducer, and a total temperature probe, consisting of two platinum thin films painted onto quartz and cordierite hemisphere cylinders. The probe diameters are 8 mm and the measurement bandwidth is 20 kHz. The objective of the present work is to develop and to demonstrate a fast response entropy probe that is of smaller dimension and larger bandwidth than the previous approaches. In this new fast-response entropy probe, the measurement of unsteady temperatures employs the use of heat transfer gauges as demonstrated by Buttsworth and Jones [5] and Chana [6]. The measurement of the pressure is based on the fast-response aerodynamic probe technology that has been developed at ETH Zurich. In the following, the design, manufacture and calibration of the probe are first presented. The purpose of the probe development is to detail the unsteady entropy field, and its associated losses, in the harsh environment of turbomachines. Thus, the application of the probe in three relevant flows—centrifugal compressor, axial turbine and film cooling flows—is also described.

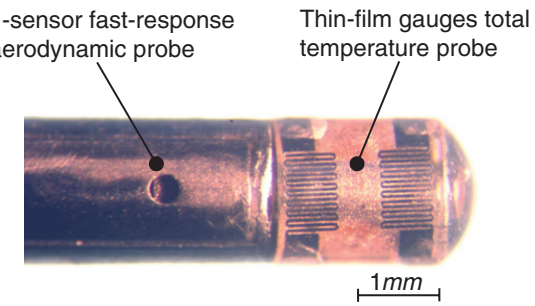

Figure 1. Photograph of the tip of the unsteady entropy probe.

2. Unsteady entropy probe

The principal components of the unsteady entropy probe (FENT) are a fast response aerodynamic probe (FRAP) and an unsteady total temperature probe, see figure 1. The diameter of the cylindrical probe is 1.8 mm, and the offset between the thin-film gauges and the pressure sensor is 2.25 mm. The design, manufacture and calibration of the FRAP are well established in the Turbomachinery Laboratory at ETH Zurich. Thus, in section 2, we discuss only the calibration of the FRAP as it is directly relevant to the FENT. Other aspects of FRAP technology are described in [7–10]. In the following, the operating principle, design, fabrication and calibration of the unsteady total temperature probe are given in detail.

2.1. Operating principal—unsteady total temperature probe

The basic element of the FENT is a pair of thin-film gauges that are deposited onto a substrate, figure 1, and operated as

Table 1. Mechanical properties (at ambient temperature) of candidate substrate materials.

	Conductivity k (W m^{-1} K^{-1})	Density ρ (kg m^{-3})	Specific heat c_p (J kg^{-1} K^{-1})	Diffusivity α (m^2 s^{-1})
PEEK	0.25	1260	2160	7.97×10^{-8}
Quartz	1.4	2200	670	9.50×10^{-7}
Macor	1.46	2520	790	7.33×10^{-7}
Silicon	130	2390	700	7.97×10^{-5}

Table 2. Electrical properties and sensitivity (at 293 K) of candidate thin-film materials.

	Resistivity r ($\mu\Omega$ cm^{-1})	TCR $\alpha_R \times 10^3$ (K^{-1})	Sensitivity $\alpha_R \times r$
Nickel	6.84	6.9	47.2
Platinum	10.6	3.93	41.7
Chromium	12.9	3	38.7

resistance thermometers. During the measurements, the thin films are operated with two different constant feeding currents; consequently, the thin-film gauges are electrically heated at two different temperatures, T_{f1} and T_{f2}. The convective heat transfer can be expressed as follows:

$$\begin{aligned} \dot{q}''_{conv1} &= h(T_t - T_{f1}) \\ \dot{q}''_{conv2} &= h(T_t - T_{f2}). \end{aligned} \tag{2}$$

The total temperature of the flow, T_t, can therefore be determined from

$$T_t = T_{f1} + \frac{\dot{q}''_{conv1}(T_{f2} - T_{f1})}{\dot{q}''_{conv1} - \dot{q}''_{conv2}}. \tag{3}$$

During the measurements, the Joule heating of the thin-film gauges is balanced by the conductive and convective heat losses. Thus, the convective heat transfer for each gauge is given by

$$\dot{q}''_{conv} = VI - \dot{q}''_{cond}. \tag{4}$$

The thin-film gauges are operated in a constant current mode, and thus the first term on the right-hand side of equation (4) is readily determined. On the other hand, the second term on the right-hand side of equation (4) is estimated by using an unsteady, semi-infinite, heat conduction model; see section 2.2.4.

2.2. Design, fabrication and calibration of an unsteady total temperature sensor

The principal requirements of the design and fabrication of the unsteady total temperature probe include integration with existing FRAP technology, robust construction for use in harsh turbomachinery environments, large measurement range for multiple applications, small sensor dimensions compatible with the FRAP's dimension, high temperature sensitivity and large frequency bandwidth (up to 48 kHz; see section 2.4.1).

2.2.1. Unsteady temperature sensor design and fabrication. The primary criteria in the selection of the material of the substrate are based on thermal properties, machinability and compatibility with the chosen fabrication technique. Among the several candidate materials given in table 1, quartz is selected due to its good machinability, low thermal conductivity and diffusivity. Although polyetheretherketone (PEEK) has a lower thermal conductivity and diffusivity than quartz, its low melting point (approximately 343 °C) is not compatible with the selected fabrication technique.

The required spatial resolution of measurements, sensitivity and time response of the temperature sensor determine the sensor geometry. Based on the experimental distribution of T_r/T_t and h on a hemisphere [11] and a cylinder [12], the thin-film gauges must be within ±25° of the stagnation point on a cylindrical probe. This placement ensures that the measured total temperature is both within 1% of the flow's total temperature and within the yaw angle calibration range (±30°) of the FRAP probe.

The temperature–resistance relationship of the thin-film gauges is expressed as

$$\frac{R}{R_{ref}} = 1 + \alpha_R(T - T_{ref}) + \beta_R(T - T_{ref})^2. \tag{5}$$

A static calibration, given in section 2.2.3, shows that the quadratic term β_R is negligible and therefore the change of the temperature coefficient is

$$\alpha_R(T) = \delta(\ln R)/\delta T. \tag{6}$$

As the thin films are operated in a constant current mode, the change in voltage across the sensor is

$$\delta V = (V\alpha_R)\delta T = (RI_e\alpha_R)\delta T. \tag{7}$$

It can be seen that the sensitivity of the sensor is proportional to both the temperature coefficient of the sensor and the excitation voltage. As the feeding current is kept constant, the sensor sensitivity is directly proportional to both the temperature coefficient of resistance and the excitation voltage. Rewriting the resistance in terms of the thin-film geometry, the sensitivity equation can be written as

$$\delta V/\delta T = (rl/wt)I_e\alpha_R. \tag{8}$$

It is evident from equation (8) that high temperature sensitivity is obtained by having a thin, narrow long film that is made from a material of high resistivity and high temperature coefficient of resistance. Table 2 shows some candidate thin-film materials. The sensitivity parameter $\alpha_R \times r$ is derived from the properties of the bulk material; however for thicknesses below 1 μm, the material's properties may differ from its bulk properties.

Nickel is selected because of its relatively high sensitivity and good adhesion characteristics in thin-film applications compared to platinum. A scale analysis of the 1D unsteady heat conduction equation gives a relation for the thermal penetration depth, equation (9). The 200 nm thick thin films are made from sputtered nickel, and thus the thin-film gauges are sufficiently thin to appear thermally transparent to unsteady temperature fluctuations up to a frequency of 580 MHz:

$$f_c = k/\rho c_p t^2. \tag{9}$$

However, it is important for sensor reliability that the bonded nickel film is stable and that its adhesion to the substrate does not deteriorate due to either intrinsic stresses or thermal

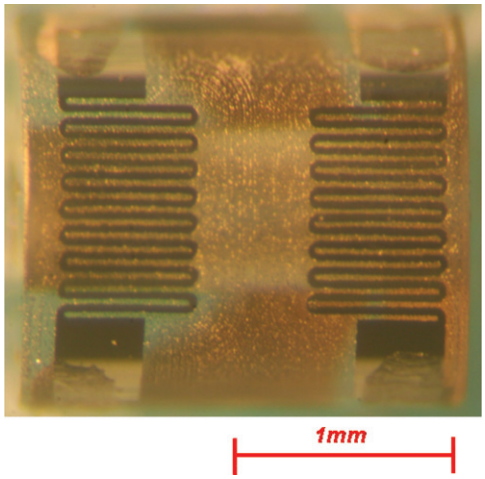

Figure 2. Unsteady total temperature probe (before integration in the FENT probe).

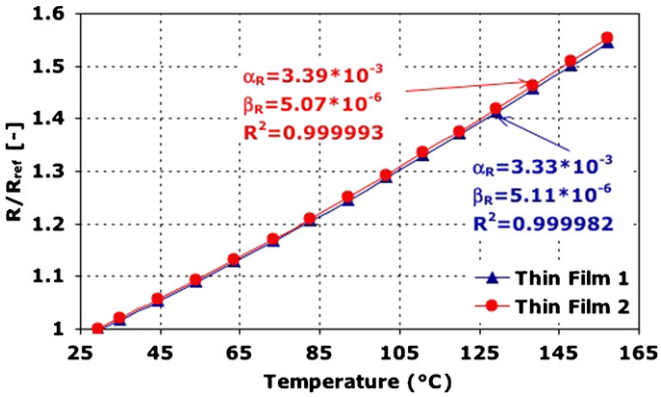

Figure 3. Resistance–temperature calibration of thin-film gauges.

stresses during measurements. The adhesion of sputtered nickel to quartz is weak as there is no chemical bonding at the film/substrate interface. This problem can be overcome by using an intermediate layer, such as chromium or titanium. As chromium has good sensitivity, a 10 nm thick chromium intermediate layer is used.

The sensor geometry is a serpentine pattern, which maximizes the sensor length and thus also maximizes the signal-to-noise ratio. As the substrate is a semi-cylindrical body, standard photolithography cannot be used. The serpentine pattern is made by removing nickel using a 20 μm diameter pulsed Nd:YAG laser beam. The resulting serpentine-shaped sensor is 30 μm wide and covers a rectangular area of 0.55 mm $\times$ 0.85 mm, see figure 2. The spatial resolution of the probe is set by the area covered by the two thin films, which is 0.85 mm $\times$ 1.77 mm. Low resistance silver leads are deposited at the ends of the sensors and run along the flat surface of the semi-cylinder; then gold wires are wedge bonded to copper wires for connection to the data acquisition system. The thin-film resistances are approximately 100 Ω.

2.2.2. Resistance–temperature calibration of thin-film gauges. A static calibration is used to derive the resistance–temperature relationship of the thin-film gauges that are operated as resistance thermometers. In the calibration, the FENT probe is exposed to a low speed (5 m s^{-1}), isothermal air stream within a channel; the air stream avoids the self-heating of the thin-film gauges and ensures that there is a homogeneous temperature field within the channel. Two thermocouples that are placed in close proximity to the probe are used to measure the temperature of the air stream. The temperature is varied over a range of 28–157 °C in steps of 10 °C, which corresponds to the temperature range of the present turbomachinery applications. The resistances of the thin-film gauges are measured after each increment when thermal equilibrium is achieved. The general form of the temperature–resistance relation is given in equation (5). Typical calibration results with a second-order polynomial curve fit are shown in figure 3. The temperature coefficients, α_r and β_r, are approximately the same for both thin-film gauges, indicating that the different steps of the manufacturing process are both well controlled and repeatable. The correlation coefficients, R^2, are 0.999 993 and 0.999 982, respectively, indicating that the curve fit is suitable for measurements. The temperature coefficient α_R is 50% of the value for bulk nickel; this difference is thought to be due to the small thickness (<1 μm) of the thin film and to the presence of the intermediate chromium adhesion layer.

2.2.3. Sensitivity to the pitch flow angle. The thin-film gauges are located 0.43 mm and 1.25 mm away from the probe tip of the 1.8 mm cylinder. Therefore, it is of interest to evaluate the effect of the pitch flow angle on the measured flow temperature. The total temperature measurements were made in the probe calibration facility that is described in [8, 15]. In this facility, probes can be calibrated in a freejet that issues from a 100 mm diameter nozzle exit. During the measurement, the flow temperature is held constant at 304 K and the pitch angle is varied over the range $-25°$ to $25°$. The effect of the pitch angle on the difference between the thin-film temperature and the flow temperature is shown for thin film 1 in figure 4(*a*). The results for thin film 2 are similar and thus not shown for lack of space. It can be seen that as the pitch angle is varied, the temperature difference varies by no more than 0.75 K over all Mach numbers. The difference between the flow total temperature with pitch and the flow total temperature at zero pitch is shown in figure 4(*b*) for $Ma = 0.3$. The deviation never exceeds 0.2 K, which leads to a relative uncertainty of $\pm 0.07\%$ in the measured total temperature. It is thus evident that over a pitch flow angle range of $\pm 25°$ relative to the stagnation point on the total temperature sensor, there is a negligible measurement error in the flow total temperature.

2.2.4. Steady and unsteady conduction to a substrate. The effect on the measured flow temperature due to steady heat conduction from the thin-film gauges to the substrate is assessed from a 3D heat transfer simulation. The commercial software ANSYS CFX is used for the simulation. The pair of thin-film gauges is simulated as constant temperature patches, whose temperature and dissipated heat flux are derived from the respective measurements. At the surface of the substrate,

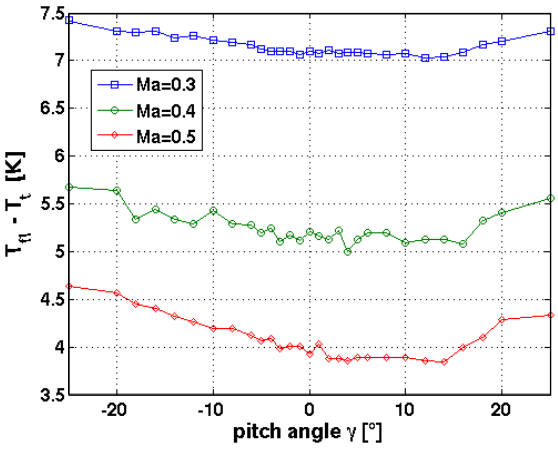

(*a*)

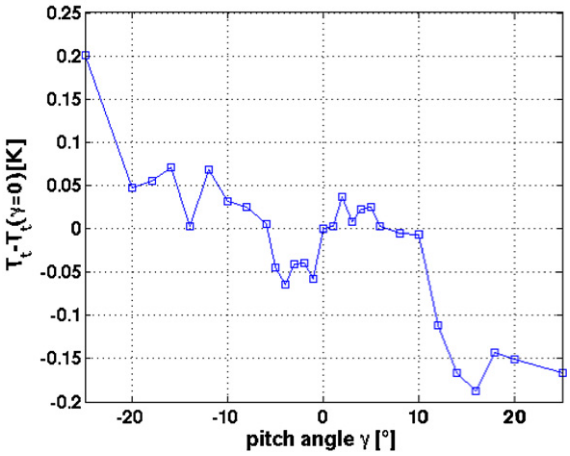

(*b*)

Figure 4. (*a*) Difference between the thin-film gauge temperature and flow total temperature for $-25^\circ < \gamma < 25^\circ$ at $Ma = 0.3$, 0.4 and 0.5. (*b*) Total temperature measurement variation for $-25^\circ < \gamma < 25^\circ$ at $Ma = 0.3$.

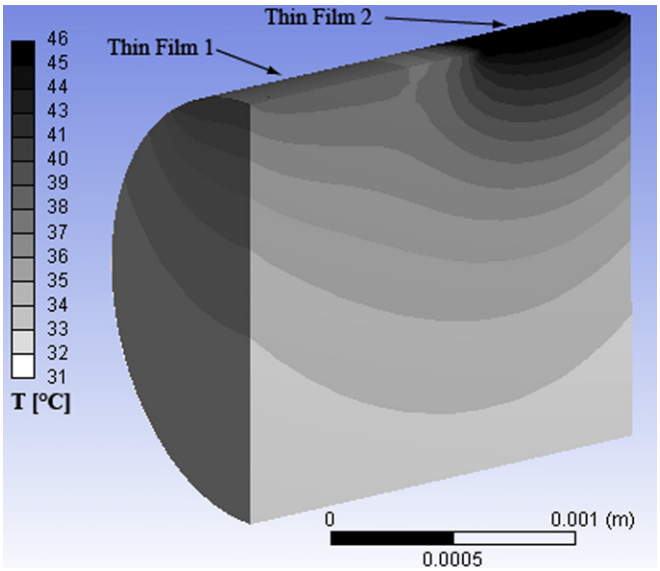

Figure 5. Steady temperature distribution through a temperature sensor quartz substrate for $Ma = 0.3$.

convective heat transfer is considered. A typical distribution of the steady temperature within the substrate is shown in figure 5. For flow Mach numbers of 0.3 and 0.6, the absolute errors in predicted flow total temperature, with and without steady conduction, are 0.82 K and 0.29 K respectively. Thus, it is concluded that the effect of steady conduction to the substrate has a negligible impact on the measured flow total temperature.

The unsteady conductive losses to the quartz substrate are estimated using an unsteady one-dimensional, semi-infinite heat conduction model. This model, which is based on the work of Schultz and Jones [13] and Oldfield *et al* [14], simulates the thermal diffusion equation using an electrical analogue. The measured thin-film voltages are numerically corrected to account for the conduction losses over the entire frequency range of interest. Thus in terms of the electrical analogue, the thermal diffusion equation (10) is written as

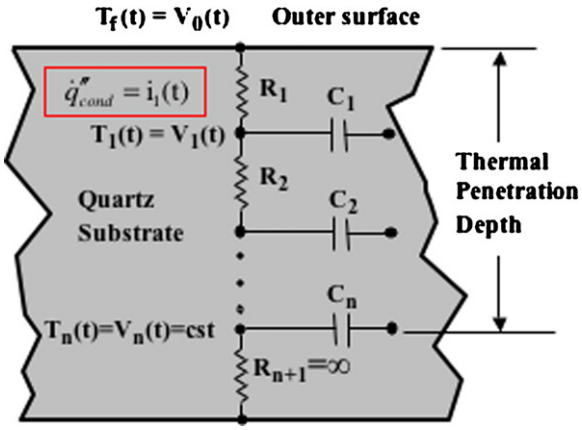

Figure 6. *RC* network analogue for conduction losses in the substrate.

equation (11):

$$\frac{\partial^2 T}{\partial x^2} = \frac{\rho c_p}{k}\frac{\partial T}{\partial t} \tag{10}$$

$$\frac{\partial^2 V}{\partial x^2} = RC\frac{\partial V}{\partial t}. \tag{11}$$

The electrical analogue is illustrated in figure 6, where the quartz substrate thermal properties are simulated using a resistance capacitance network. The voltage, V, capacitance, C, and resistance, R, are analogous to temperature, T, thermal resistance, $\Delta x/k$, and thermal conductance, $\rho c_p \Delta x$, respectively. As suggested by Oldfield *et al* [14], the resistances and capacitances are weighted logarithmically in a manner that is analogous to the logarithmic spacing between nodes that are 'placed' across the thermal penetration depth within the substrate. Therefore, an order of magnitude fewer series resistances and capacitances can be used to accurately predict the conductive losses than if a linear spacing is used.

The discretized set of equations

$$\frac{\partial V_i}{\partial t} = \frac{V_{i-1}}{R_i C_i} - \frac{V_i}{C_i}\left(\frac{1}{R_i} + \frac{1}{R_{i+1}}\right) + \frac{V_{i+1}}{R_{i+1}C_i} \tag{12}$$

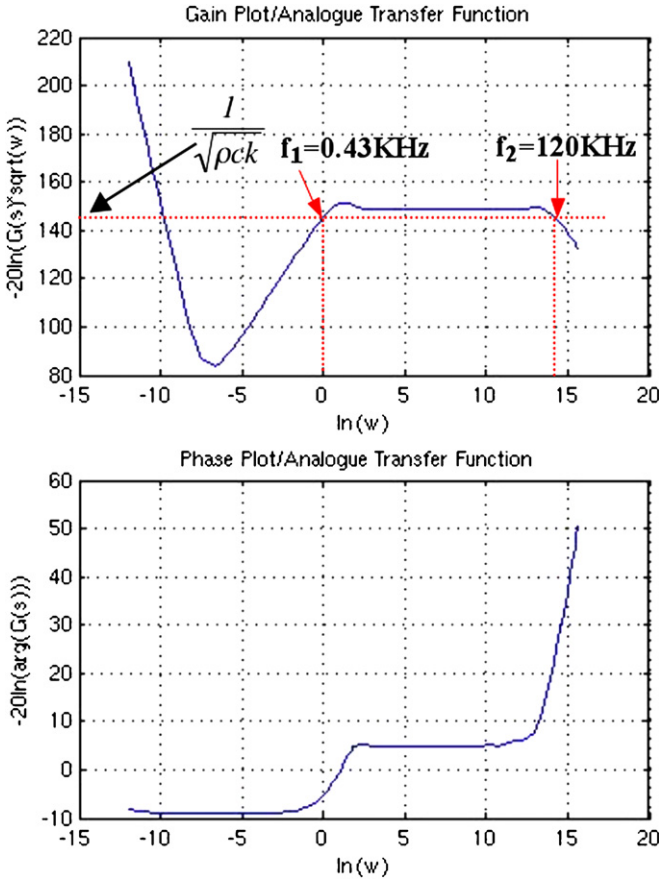

Figure 7. Conduction model transfer function: amplitude (top) and phase (bottom).

are solved using a fourth-order Runge–Kutta method. The boundary conditions for equation (12) are derived from the temperatures of the thin-film gauges at the surface $T_f(t)$ and the assumption of a zero unsteady heat flux at the depth of thermal penetration. The latter condition is imposed by setting the resistance R_{n+1} to infinity. As suggested in [13], the unsteady thermal penetration depth x, equation (13), is calculated based on the thermal diffusivity and the frequency of interest. In the present work, the blade passing frequency is the frequency of interest:

$$x = 4\sqrt{\frac{a}{f}}. \tag{13}$$

A linear temperature distribution across the thermal penetration depth is assumed in order to provide an initial condition, and the last node temperature $T_n(t)$ is set to the average measured surface temperature $\bar{T}_f(t)$.

The frequency response of the electrical analogue is iteratively determined from

$$\begin{aligned} Z_N &= R_N + \frac{1}{j\omega C_N} \\ Z_i &= R_i + \frac{Z_{i+1}}{j\omega C_i Z_{n+1}}, \qquad i = (n-1), \ldots, 2, 1. \end{aligned} \tag{14}$$

The conduction model transfer function of the substrate model, plotted in figure 7, is expressed in equation (15):

$$G(s) = \frac{T(s)}{q(s)} = \frac{1}{\sqrt{\rho ck}\sqrt{s}}. \tag{15}$$

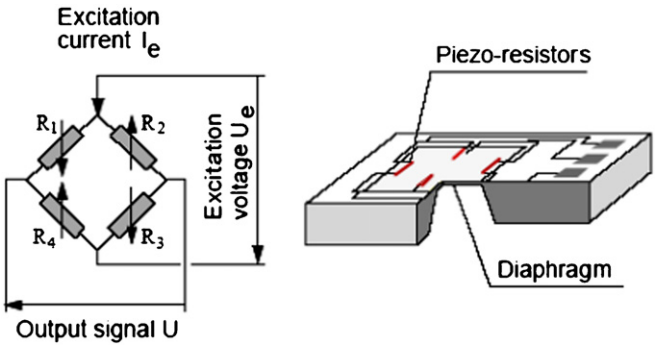

Figure 8. Schematic of the Wheatstone bridge and miniature silicon piezoresistive pressure sensor chip used in the FRAP.

The frequency response of the conduction model determines the frequency response of the total temperature measurements. The bandwidth of the model used in the present work is 0.43 Hz–120 kHz. This upper frequency is less than the cut-off frequency of the thin film alone. The phase shift of the conduction model is less than 5°, which ensures that the bandwidth of the measured total temperatures covers that of the total pressures.

2.3. Fast response aerodynamic probe

A one-sensor fast response aerodynamic probe (1S-FRAP) is used to measure the time-resolved pressures. The FRAP employs a miniature silicon piezoresistive chip, figure 8, that is glued beneath a pressure tap on the probe tip. A constant excitation current I_e is provided to the Wheatstone bridge to induce an excitation voltage U_e and an output signal voltage U. The output signal is strongly dependent on the pressure differential across the chip and is only weakly dependent on temperature; on the other hand, the excitation voltage is weakly dependent on the pressure and more strongly dependent on the temperature.

Figure 9 shows the calibration of the piezoresistive sensor over a range of pressures (0–570 mbar) and temperatures (40–130 °C). As described above, the output signal U is weakly temperature dependent, while the excitation signal U_e is decoupled from the pressure. For the measurements, a polynomial interpolation, equation (16), is used to determine the pressure and temperature from the measured sensor signals:

$$\begin{aligned} p(U, U_e) &= \sum_{i=0}^{m}\sum_{j=0}^{n} K_{p_{i,j}} U^i U_e^j, \\ T(U, U_e) &= \sum_{i=0}^{m}\sum_{j=0}^{n} K_{T_{i,j}} U^i U_e^j. \end{aligned} \tag{16}$$

The 1S-FRAP is calibrated and operated in a virtual three-sensor mode by turning the probe to three positions, as shown in figure 10. A set of three dimensionless calibration coefficients, given in equation (17),

$$K_\varphi = \frac{p_2 - p_3}{p_1 - p_m}, \qquad K_t = \frac{p_{tot} - p_1}{p_1 - p_m}, \qquad K_s = \frac{p_1 - p_{stat}}{p_1 - p_m}, \tag{17}$$

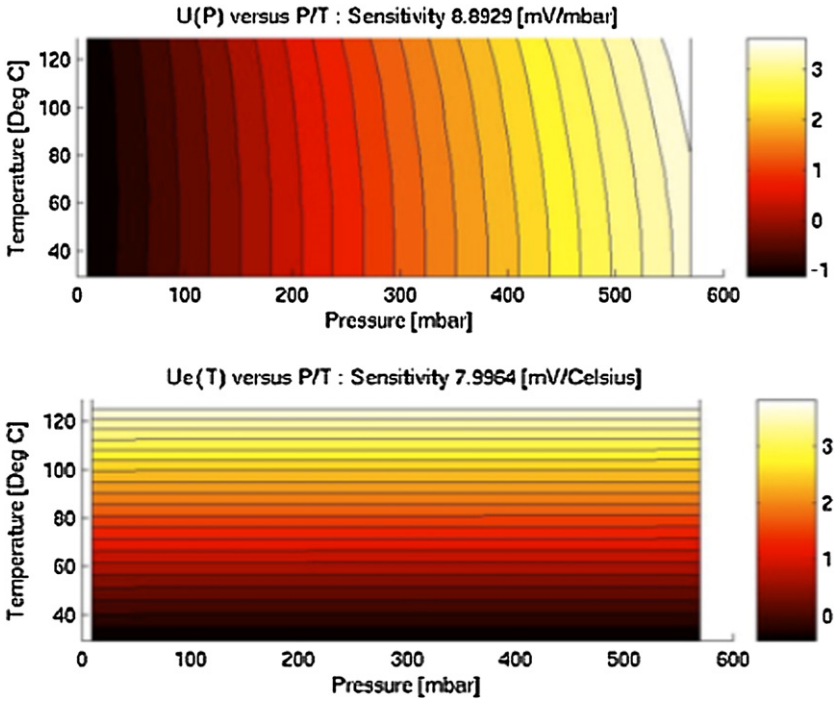

Figure 9. Calibration of the piezoresistive sensor output signal U and excitation signal U_e as a function of pressure and temperature.

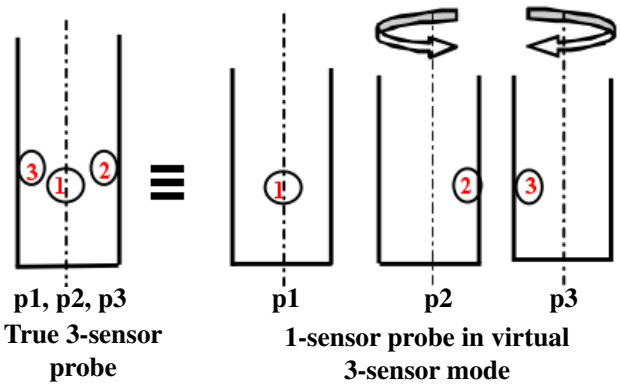

Figure 10. 1S-FRAP virtual three-sensor mode concept.

where $p_m = (p_2 + p_3)/2$, is determined from the calibration and then subsequently used to determine the yaw angles and velocities [15].

The temperature of the encapsulated sensor of the 1S-FRAP is evaluated from the sensor signal U_e. This measured temperature has a frequency bandwidth of less than 10 Hz due to the thermal inertia of the chip. However, this temperature is not a measure of the flow total temperature since the heat dissipated by the sensor causes an increase in the temperature of membrane relative to the flow's static temperature. Moreover, due to the proximity of the thin-film gauges, the heating effect of the thin-film gauges on the piezoresistive sensor must be accounted for. The sensor and the flowfield temperatures can be related by using an effective recovery factor [16]. The effective recovery factor represents the ratio of the measured enthalpy difference on the adiabatic wall to the enthalpy difference of the stream, equation (18):

$$r = \frac{\Delta h_i}{\Delta h_t} = \frac{h_i - h_s}{h_t - h_s} = \frac{T_{aw} - T_s}{T_t - T_s}. \tag{18}$$

Using the definition of total temperature, equation (19),

$$T_t = T_s + \frac{v^2}{2c_p} \tag{19}$$

and substituting the adiabatic wall temperature, T_{aw}, with the temperature of the encapsulated sensor, T_i, the effective recovery factor can be written as equation (20):

$$r = 1 - \frac{2c_p}{v^2}(T_t - T_i). \tag{20}$$

This measured effective recovery factor is used to correct the temperature measured with the piezoresistive sensor of the FENT probe. The probe calibration facility described in [8, 15] is used to evaluate the temperature difference (and thus the effective recovery factor) as given in equation (20). Figure 11 shows the total temperature difference between the flow total temperature and the piezoresistive sensor's temperature, derived from measurements, with and without the thin-film gauges in operation, over the Mach number range 0.1–0.7.

2.4. Dynamic response

2.4.1. Fast response aerodynamic probe. The dynamic response of the pressure signal depends on the dynamic properties of the sensor diaphragm and the sensor's position relative to the pressure tap. The dynamic response of the pressure signal has been measured in the freejet facility [8, 15], equipped with a fine mesh grid. The resulting flow turbulence has a constant amplitude over relatively low frequencies and

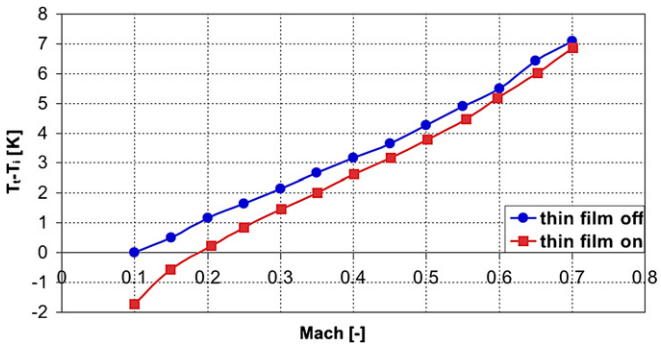

Figure 11. Effect of the thin-film gauge operation on the total temperature derived T_i from the piezoresistive sensor in the FENT probe.

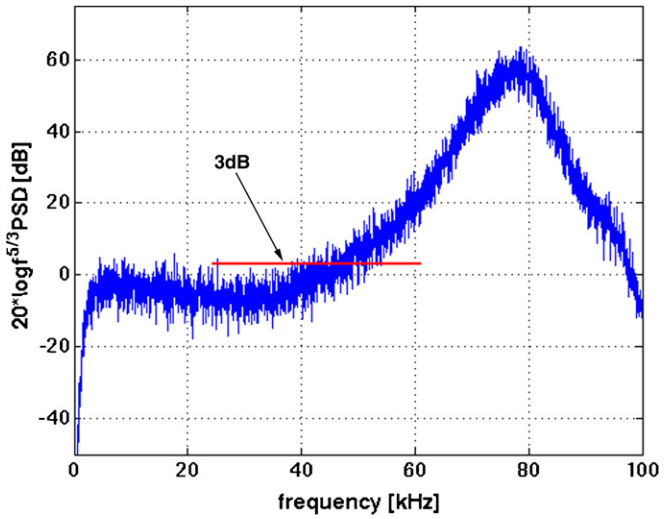

Figure 12. Amplitude response of the 1S-FRAP. The measured response is from grid-generated turbulence.

then decays with a characteristic slope of $-5/3$ at higher frequencies. The amplitude response in terms of $f^{5/3}P(f)$ versus frequency is shown in figure 12. The peak at 75 kHz corresponds to the eigenfrequency of the pneumatic cavity. The amplitude is flat up to a frequency of 48 kHz, above which the amplitudes are in excess of 3 dB. Thus, the cut-off frequency of 48 kHz determines the measurement of the bandwidth of the FENT probe.

2.4.2. Fast response total temperature probe dynamic response. The dynamic response of the total temperature sensor has been assessed from measurements in the inlet to the first rotor stage of an axial research turbine facility. The facility is described in section 5.3. In the freestream, upstream of the rotor, isentropic fluctuations of temperature and pressure occur due to the rotor's potential field. The total temperature and total pressure fluctuations measured upstream of the rotor leading edge are shown in figure 13. The blade passing frequency is 2450 Hz, and the temperature and pressure are normalized with respect to their values at the turbine inlet, equations (21) and (22). The normalized pressure is raised to an exponent $(\gamma - 1)/\gamma$, so that the isentropic variation can be assessed:

$$\hat{T} = \frac{T_t}{T_{t,ref}} \tag{21}$$

$$\hat{p} = \left(\frac{p_t}{p_{t,ref}}\right)^{\gamma-1/\gamma}. \tag{22}$$

The two measurements show good overall agreement, see figure 13. This result gives a high degree of confidence in the measurement of unsteady temperature, as well as the derived entropy generation.

3. Measurement system

The measurement system consists of the FENT probe, an integrated signal conditioner, a multi-axis probe traversing system and a laboratory PC that is equipped with two NI-DAQ four-channel data acquisition boards. Four signals from the probe (U and U_e from the FRAP and U_{f1} and U_{f2} from the thin-film gauges) and a trigger signal are simultaneously acquired at a sampling rate of 200 kHz. Following data acquisition, the FRAP and thin-film gauge signals are processed, in parallel, prior to being recombined to yield the relative entropy. For the thin-film gauges, the resistance–temperature calibration is first calculated, and then the conduction model is applied to determine the corrected unsteady total temperature. For the FRAP, the static calibration of the piezoelectric sensor and then aero-calibration are applied. All the computations are performed in the MATLAB environment. The measurement grid has a radial spacing of 1.125 mm in the regions of clustering and of 2.25 mm elsewhere. In data processing coincident phase-locked measurements of p_t and T_t are used to determine the unsteady relative entropy. A schematic diagram of the measurement system is shown in figure 14.

4. Uncertainty analysis

The measurement uncertainties related to the measurements using the newly designed unsteady total temperature sensor are first addressed. Then the absolute uncertainties of the derived entropy production are given for the three test rigs, where the measurements are conducted. The measurement uncertainty derivation is based on the absolute error propagation equation (23):

$$\Delta F = \pm\sqrt{\left(\frac{\partial F}{\partial x}\cdot\Delta x\right)^2 + \left(\frac{\partial F}{\partial y}\cdot\Delta y\right)^2 + \cdots}$$
$$\text{with} \quad F = f(x, y, \ldots). \tag{23}$$

4.1. Unsteady total temperature measurement uncertainty

The derivation of the unsteady total temperature is based on equation (3). Therefore, the uncertainty in the unsteady total temperature measurements depends on the uncertainties associated with the measurements of the thin-film total temperatures (T_{f1}, T_{f2}) and the convective heat transfer rates ($\dot{q}''_{conv1}$, $\dot{q}''_{conv2}$). Thus, equation (24) defines the absolute error

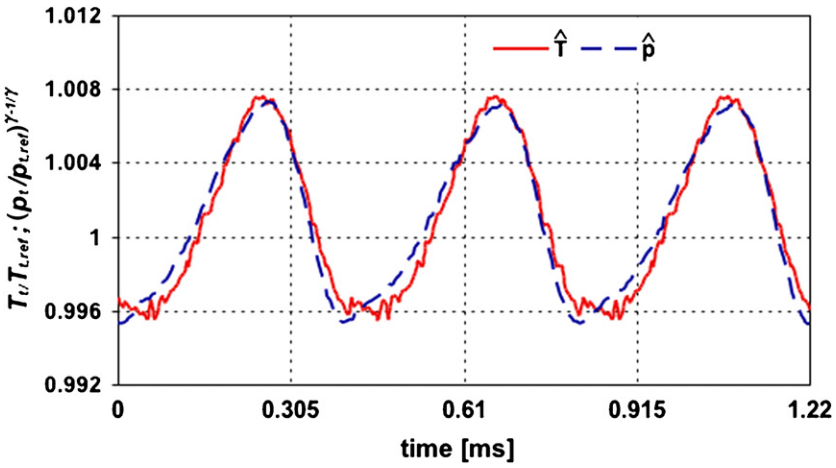

Figure 13. Comparison of the measured total temperature and the scaled total pressure at the rotor inlet of the first stage of an axial turbine.

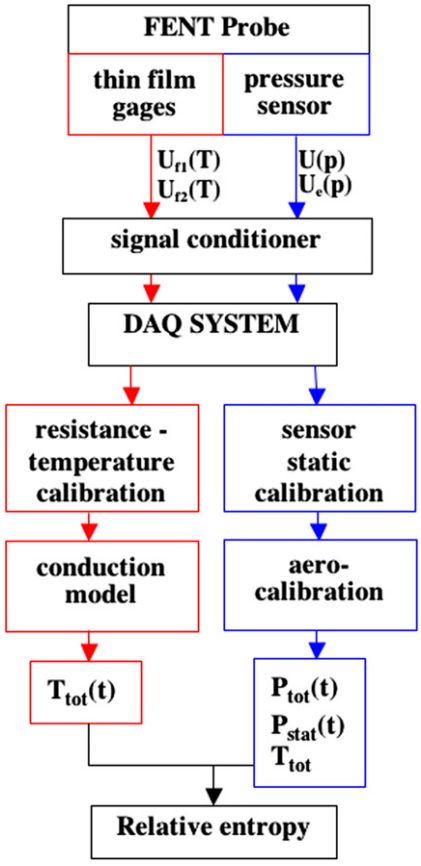

Figure 14. FENT probe measurement chain and data processing.

in the measured total temperature:

$$\Delta T_t = \pm\left[\left(\frac{\dot{q}''_{conv2}}{\dot{q}''_{conv1}-\dot{q}''_{conv2}}\Delta T_{f1}\right)^2+\left(\frac{\dot{q}''_{conv1}}{\dot{q}''_{conv1}-\dot{q}''_{conv2}}\Delta T_{f2}\right)^2+\left(\frac{\dot{q}''_{conv2}(T_{f1}-T_{f2})}{(\dot{q}''_{conv1}-\dot{q}''_{conv2})^2}\Delta\dot{q}''_{conv1}\right)^2+\left(\frac{\dot{q}''_{conv2}(T_{f2}-T_{f1})}{(\dot{q}''_{conv1}-\dot{q}''_{conv2})^2}\Delta\dot{q}''_{conv2}\right)^2\right]^{1/2}. \quad (24)$$

Table 3. Sources of uncertainty related to the measured total temperature.

Source of uncertainty	Parameter X	Relative uncertainty $\Delta X/X$ (%)
Density (quartz)	ρ	±0.5
Specific heat (quartz)	c_p	±2
Conductivity (quartz)	k	±3
Thin-film temperature	T_f	±1

The error related to the second-order polynomial curve fit of the thin films' temperature–resistance calibration is negligible; see section 3.3.1. Due to spatial variations of the air temperature in the temperature–resistance calibration facility and uncertainties in the thermocouple calibration, the output voltage of the constant current electrical circuit $\Delta V/V$ and the measurement of the ambient film temperature, the relative error in the measured thin-film gauge temperatures is estimated as $\Delta T_f/T_f = 1\%$.

The uncertainty for the convective heat transfer comes from the model of the unsteady conduction losses, equation (10). The uncertainty in the unsteady conduction, equation (25), depends on the measured thin-film temperature and the thermal properties of the fused quartz material. As presented in [5], the density of quartz is taken as 2200 kg m^{-3}, since quoted values for fused quartz vary between 2190 and 2210 kg m^{-3}. Therefore, the relative uncertainty in the density is $\Delta\rho/\rho = \pm 0.5\%$. The uncertainties in the curve fits for the conductivity and the specific heat of fused quartz are $\Delta k/k = \pm 3\%$ and $\Delta c_p/c_p = \pm 2\%$, respectively. These uncertainties yield relative uncertainty in the convective heat flux $\Delta\dot{q}''_{conv}/\dot{q}''_{conv}$ of ±3.77%; the sources of uncertainty are summarized in table 3:

$$\frac{\Delta\dot{q}''_{conv}}{\dot{q}''_{conv}} = \left[\left(\frac{\Delta T_f}{T_f}\right)^2+\left(\frac{\Delta\rho}{\rho}\right)^2+\left(\frac{\Delta c_p}{c_p}\right)^2+\left(\frac{\Delta k}{k}\right)^2\right]^{1/2} = 3.77\%. \quad (25)$$

The temperature and convective heat transfer conditions differ from one test facility to another as the flow conditions are different. Table 4 summarizes the absolute and relative

Table 4. Measurement uncertainties in the total temperature of the three facilities.

Facility	Absolute uncertainty, ΔT_0 (K)	Relative uncertainty, $\Delta T_0/T_0$ (%)
RIGI	±8.47	±2.43
LAVAL	±9.30	±2.49
LISA	±7.33	±2.42

Table 5. Measurement uncertainties in the reference conditions and relative entropy of the three test facilities.

Test rig	Δp_{REF} (Pa)	ΔT_{REF} (K)	$\Delta(\Delta s)$ (kJ kg^{-1})
RIGI	±120	±0.2	±7.80
LAVAL	±140	±0.9	±10.42
LISA	±14	±0.4	±7.51

measurement errors in relative entropy for the three facilities that are used in the present work.

4.2. Uncertainty in entropy

Since entropy can only be inferred from other properties, the measurement uncertainty of the entropy probe can only be evaluated in terms of the measurement errors in these other properties. Four properties, the measured total pressure and total temperature and their respective reference values, are used to determine the entropy, equation (1). The uncertainty in the measured total pressure is in the range ±100 Pa [9], whereas the absolute uncertainty in the unsteady total temperature differs between the measurement devices of the test facilities as given in table 4. The absolute error of the reference conditions differs from one test facility to another as the measurement devices are different. The respective absolute errors of the reference conditions in the radial compressor 'RIGI', in the film cooling facility 'LAVAL' and axial turbine 'LISA' are given in [17, 18, 10]. Table 5 summarizes the relative measurement errors for the three facilities that are used in the present work.

5. Application of the fast entropy probe

5.1. Measurements in a centrifugal compressor

Measurements using the FENT probe are first presented from the single stage, centrifugal compressor system, 'RIGI', at ETH Zurich. This facility is described in detail in [19]. For the present tests, the system is equipped with a centrifugal impeller followed by a vaneless diffuser. The impeller is typical of that found in small-scale distributed power generation and automotive turbocharging applications [20]. The impeller has seven pairs of full and splitter blades, as shown in figure 15. Its outer diameter is 400 mm, and at the impeller exit the blades are swept back by an angle of 30° with respect to the radial direction. The measurements were conducted at the blade tip Mach number $Mu = 0.8$, which corresponds to a blade passing frequency of 3026.8 Hz. Immediately downstream of the impeller is a parallel vaneless diffuser with an exit diameter of 580 mm; the diffuser height is 15.7 mm. The clearance ratio,

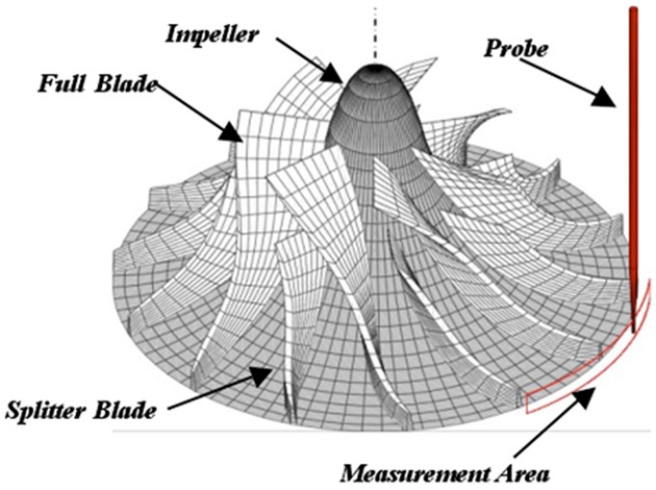

Figure 15. Impeller of the centrifugal compressor showing the probe location and measurement area.

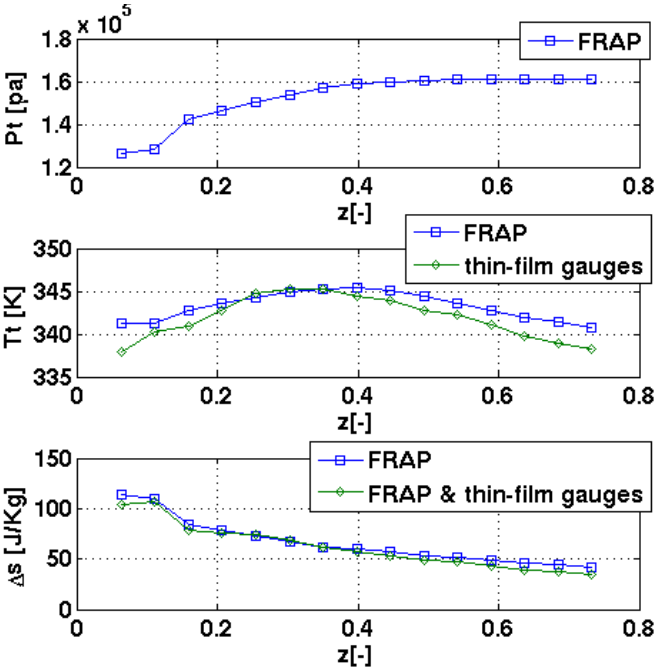

Figure 16. Circumferentially averaged profiles of the total pressure, total temperature and entropy.

which is defined as the ratio of the tip gap width 0.7 mm to the diffuser height 15.7 mm, is 4.5%. The measurements are made at a radial position of $R_{\mathrm{d}}/R_{\mathrm{d2}} = 105\%$. The spatial resolution of the measurements is 1.77 mm in the axial direction and 0.39° azimuthally. The stage inlet reference conditions are $p_{\mathrm{ref}} = 95\,830$ Pa and $T_{\mathrm{ref}} = 297$ K.

The circumferentially averaged measurements of pressure, temperature and entropy are presented in figure 16. As can be seen, the profiles of the measured temperatures agree very well over the diffuser height. Quantitatively, the differences between the two measurements are no more than 0.8%; this excellent agreement is validation of the FENT probe's design. Also shown in figure 16 is the total pressure distribution that is derived from the FRAP component of the

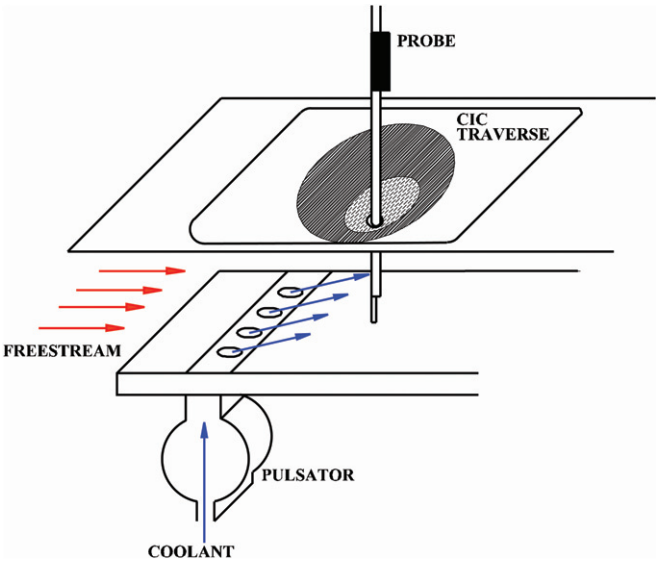

Figure 17. Schematic of the measurement section of the film cooling facility LAVAL.

FENT probe. This distribution shows that there are lower total pressures near the shroud wall compared to the hub wall; this suggests that there are more losses in the flow that is adjacent to the shroud. The measured entropy profiles, also shown in figure 16, confirm this observation. It should be noted that there are two relative entropy profiles, each derived from the total temperatures measured using the piezoresistive sensor of the FRAP and thin-film gauges. The two profiles show excellent agreement with each other. More complete details of the measurements are reported in [21].

5.2. Measurements in the film cooling facility

A second series of measurements performed in the film cooling facility Laval at ETH Zurich, are next presented. This facility is designed to give quantitative measurements related to the aerothermal effectiveness of different film cooling configurations. A schematic of the facility is shown in figure 17. As described by Bernsdorf *et al* [18], the facility consists of a closed loop wind tunnel, which drives the main flow, and a pulsator, which delivers the coolant flow. The test section has a rectangular flow path of 40×181 mm^2 and the diameter of the injection hole is $D = 7$ mm. The test conditions for the present measurements are the freestream Mach number of $Ma = 0.3$ and mean blowing ratios BR $=$ 1 and 2. The density ratio is DR $= 1.29$, which corresponds to a 90 °C temperature difference between the freestream and the coolant. The pulsation frequency is $f_c = 400$ Hz, which corresponds to a Strouhal number based on the hole diameter of $St = 0.025$. A four-axis traversing system, based on a two non-concentric circle-in-circle (CIC) arrangement, provides for probe measurements along streamwise and crosswise measurement planes. In the cross plane, the measurement grid is comprised of 15 equally spaced points in the vertical direction, and in the lateral direction 19 points that are clustered close to the centre of the injection holes.

The unsteady thermal field, in terms of the normalized total temperature Θ, for BR $= 1$ and 2 at $X/D = 6$ is shown in figure 18. For the blowing ratio BR $= 1$, the jet is always in contact with the surface; thus, there is continuous cooling of the surface. On the other hand, for BR $= 2$, the jet detaches from the surface and thus the film cooling effectiveness is reduced. Moreover, at this higher blowing ratio, the coolant jet breaks up into a counter-rotating vortex pair, the symmetric cores of which contain the coolest flow. This shows that the temperature mixing is primarily driven by the counter-rotating vortex pair rather than being associated with the unsteadiness of the pulsation. Although the position of the cores varies with time, the detachment from the surface of the coolant is an indicator of poor average cooling effectiveness, as the counter-rotating vortex pair tends to confine warmer fluid from the freestream under the jet. These experimental results, in parallel with predictions of the time-resolved measurement of the thermal field [22], provide a better understanding of the influences of the pulsation and mean blowing ratio on the temperature distribution and the film cooling effectiveness.

The instantaneous ($\Delta t/\Delta t_{per} = 0.75$) normalized temperature and its corresponding entropy function distribution at the distance $X/D = 6$ for BR $= 2$ are shown in figure 19. The freestream inlet conditions are taken as reference values. As pressure measurements could not be performed for $Z/D < 0.47$, the boundary layer is not captured in the entropy measurements. The similarity of entropy contours to the temperature gradients suggests the preponderance of the temperature gradients over the pressure gradients in entropy generation. Three main flow regions can be identified: the freestream in which there is no entropy generation, the shear layer in which there is moderate entropy generation and the counter-rotating vortex pair within which there is the highest level of entropy generation. The generation of entropy in the shear layer region is mainly due to small-scale mixing, whereas the larger generation of entropy in the counter-rotating vortex pair is due to the entrainment as a result of the large vorticity. More details of the entropy distribution and aerothermal performance are presented in [23].

5.3. Measurement in the axial turbine facility 'LISA'

A third set of measurements to demonstrate the capability of the FENT probe is performed in the axial research turbine 'LISA'. For the present measurements, the facility was equipped with a 1.5 stage of an axial turbine that is described in [24]. The measurements were performed at a rotor speed of 2700 rpm, which corresponds to a rotor blade passing frequency of 2430 Hz. The operating parameters for the present measurements are summarized in table 6. The measurements presented here were made 15% rotor axial chord downstream of the rotor trailing edge, see figure 20. The measurement grid is comprised of 27 points in the radial direction clustered close to the end-walls and in the circumferential direction 20 equally spaced points that cover 1 stator pitch. The data are processed by applying a phase lock average over 85 rotor revolutions.

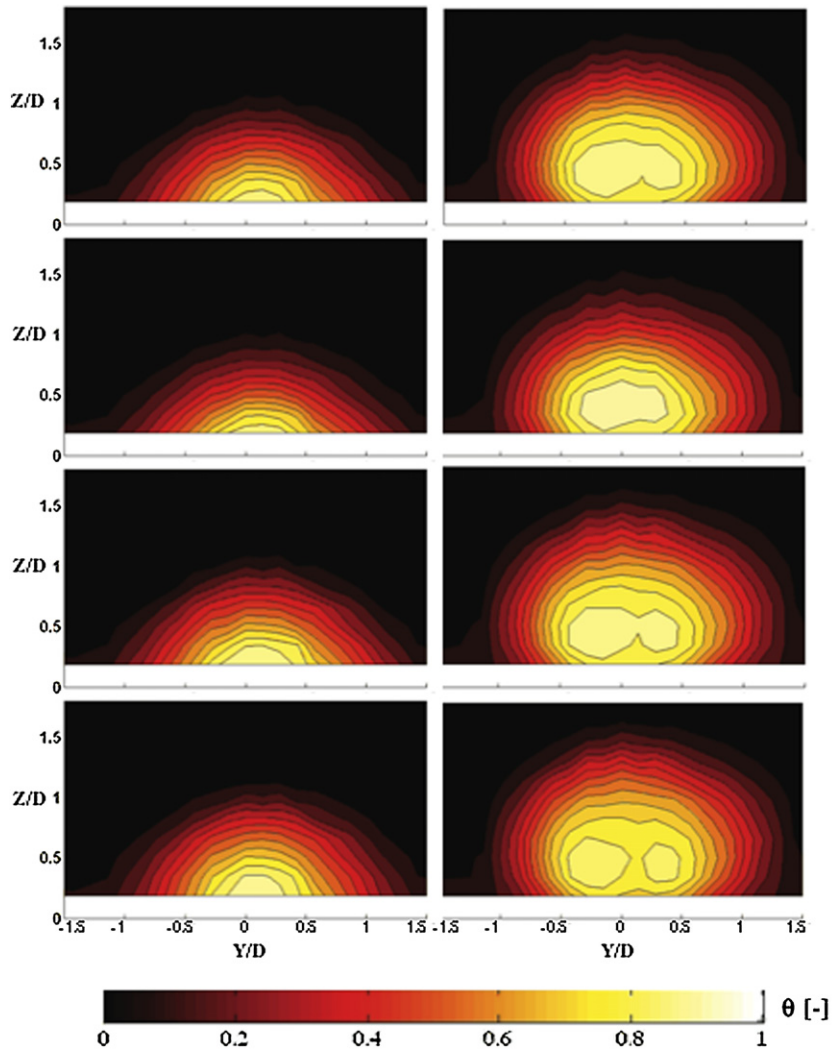

Figure 18. Measured time-resolved ($\Delta t/\Delta t_{per} = 0.00, 0.25, 0.50, 0.75$) normalized temperature field, θ, at the cross plane $X/D = 6$. BR = 1 (left column) and BR = 2 (right column).

Table 6. Main parameters of 'LISA' 1.5-stage axial turbine research.

Rotor speed (rpm)	2700
Number of rotor blades	54
Rotor blade passing frequency (Hz)	2430
Pressure ratio (1.5-stage, total-to-static)	1.60
Turbine entry temperature (°C)	55
Total inlet pressure (bar abs norm)	1.4
Mass flow (kg s^{-1})	12.13
Shaft power (kW)	292
Hub/tip diameter (mm)	660/800
Rotor axial chord (mm)	46

The most commonly used measurement of the loss coefficient for a turbine blade row is the stagnation pressure loss coefficient that is given as

$$Y = \frac{P_{t1} - P_{t2}}{P_{t2} - P_2}. \tag{26}$$

The loss definition is widely used because it is easily measurable, but it is of limited utility as it implies a constant total temperature. This is not realistic for a rotating blade row and multi-stage axial turbines, where the rotor blades' secondary flow and the downstream stator blades' potential field cause strong temperature variations at the rotor exit [25]. A more appropriate measurement of the turbine blade row loss is the entropy loss coefficient that is given as

$$\zeta = \frac{T_2 \Delta s}{h_{t2} - h_2}. \tag{27}$$

The measurements of the entropy loss coefficient in the present work are shown in figure 21. Due to the fact that this test rig is equipped with low aspect ratio blading, the secondary flows extend over a wide range between the casing and the hub. The tip leakage vortex is centred at 95% span and is seen to be the dominant loss core. The upper and lower passage vortices, respectively centred at 80% and 25% spans, are seen to be regions of intermediate loss. The wake extends over the mid-span and is a region of low entropy creation. The remainder of the flowfield is occupied by the almost loss-free freestream.

An advantage of the entropy measurement is that it can be converted into the practically relevant measure of efficiency, as follows:

$$\eta = \frac{h_1 - h_2}{h_1 - h_2 - T_2 \Delta s}. \tag{28}$$

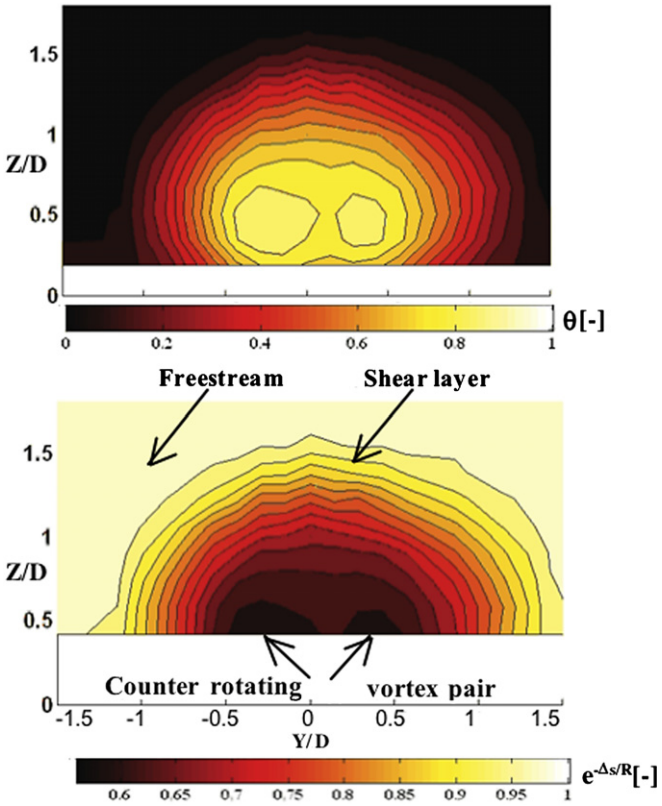

Figure 19. Measured normalized temperature, θ (top), and entropy function field, $e^{-\Delta s/R}$ (bottom), at $X/D = 6$. BR $= 2$, DR $= 1.29$ and $\Delta t/\Delta t_{per} = 0.00$.

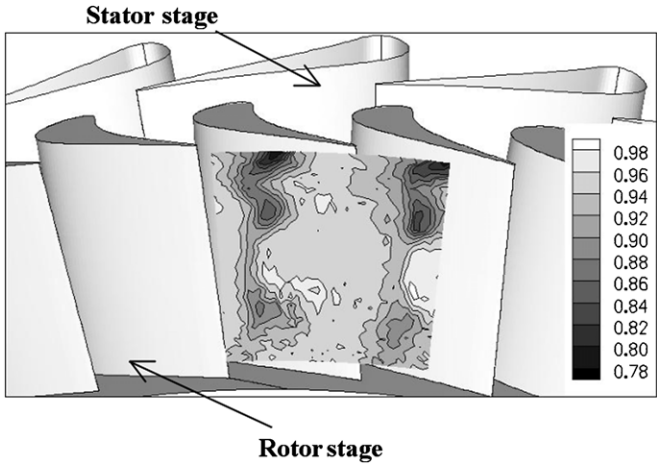

Figure 20. Entropy distribution at the rotor exit of the 1.5 stage axial turbine research turbine facility 'LISA'.

Figure 22 shows the distribution of efficiency in the measurement plane, and in table 7 the ratio of the minimum-to-maximum efficiencies in the four previously identified secondary flowfield structures is summarized. The tip leakage vortex has the lowest efficiency ratio of 28.3%. The hub passage vortex has an efficiency ratio of 48.4%, whereas the lower passage vortex has an efficiency ratio of 53.5%. The wake is the secondary flow structure that shows the highest efficiency of 75.8%. These measurements of efficiency

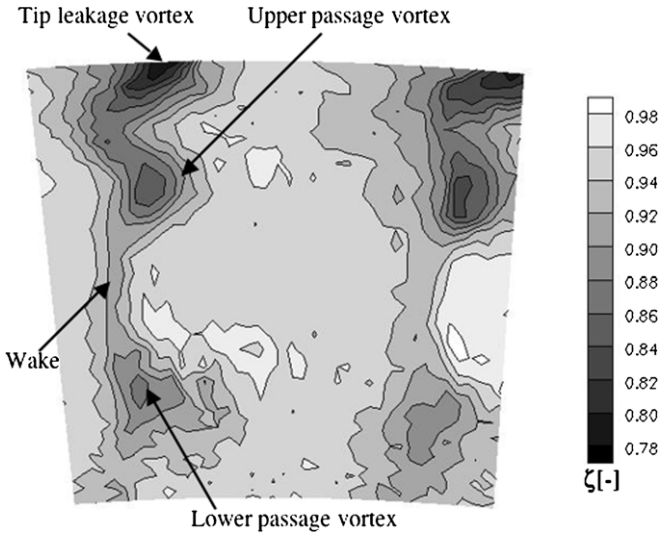

Figure 21. Distribution of the measured entropy loss coefficient, ζ, at the rotor exit.

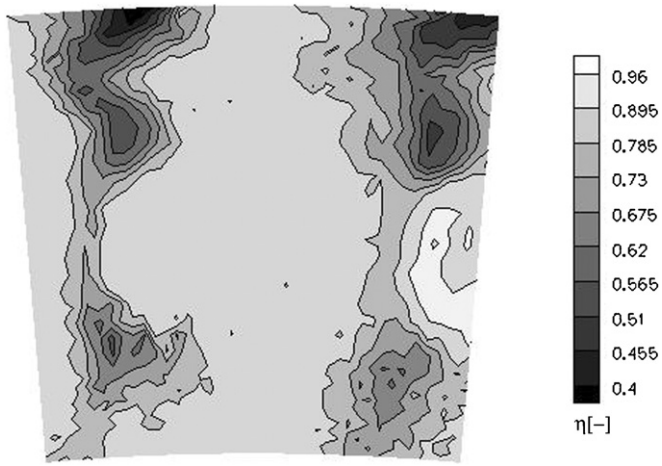

Figure 22. Distribution of the measured entropy efficiency, η, at the rotor exit.

Table 7. Efficiency ratio in the secondary flow regions identified in figure 21.

Secondary flows	η_{min}/η_{max}
Tip leakage vortex	28.3
Upper passage vortex	53.5
Wake	75.8
Lower passage vortex	48.4

clearly show that the tip leakage vortex is the main source of aerodynamic loss and that an approach to improve the efficiency can be to reduce the tip leakage mass flow. Furthermore, the entropy measurement confirms that for a low aspect ratio turbine, the interaction of the secondary flow with the free stream is more important than that caused by the wakes. More details of this analysis are presented in [25].

6. Conclusion

A fast response entropy probe (FENT) has been designed, built and used to make measurements in three facilities: a

radial compressor, a film cooling facility and an axial turbine. The principal components of the miniature (diameter 1.8 mm) FENT are a fast response aerodynamic probe (FRAP) and an unsteady total temperature probe based on thin-film technology. The thin-film gauges are fabricated by sputtering 200 nm thick nickel in a serpentine shape onto a 1.8 mm semi-cylindrical quartz substrate. This design provides high spatial resolution, high temperature sensitivity and robustness, which ensures that the unsteady total temperature measurement capability is in the same range as that of the unsteady total pressure.

The thin-film gauges do not require an extensive calibration procedure, as a static calibration is used to derive the thin-film resistance–temperature relationship for the thin-film gauges that are operated as resistance thermometers. An unsteady, semi-infinite, heat conduction model is used to correct for the heat losses to the substrate. The bandwidth of the model used in the present work is 0.43 Hz–120 kHz with a phase shift of less than 5°. However, the FRAP that is integral to the FENT probe limits the frequency of the FENT probe to 48 kHz.

The application of the probe in several facilities has proven the robustness of the FENT probe in flows including a high Mach number and large temperature gradients. These applications show that this miniature, fast-response entropy probe can provide new insight into the loss generation mechanisms.

Acknowledgments

The authors acknowledge the support of Albert Kammerer, Vipluv Aga and Peter Schüpbach for their assistance in conducting the measurements in the radial compressor 'RIGI', the film cooling facility 'LAVAL' and axial turbine 'LISA' respectively. The authors also thank Cornel Reshef for his work in developing the electronic instrumentation and data acquisition system for the unsteady entropy probe, and gratefully acknowledge his continuous support for the development of FRAP and other fast response measurement techniques at ETH Zürich over the last 20 years.

References

[1] Denton J D 1993 Loss mechanisms in turbomachines *ASME J. Turbomach.* **115** 521–652

[2] Ng W F and Epstein A H 1983 High-frequency temperature and pressure probe for unsteady compressible flows *Rev. Sci. Instrum.* **54** 1678–83

[3] Payne S J, Ainsworth R W, Miller R J, Moss R W and Harvey N W 2003 Unsteady loss in a high pressure turbine stage *Int. J. Heat Fluid Flow* **24** 698–708

[4] Passaro A, LaGraff J E, Oldfield M L G, Biagioni L, Moss R W and Battelle R J 2003 Measurements of turbulent pressure and temperature fluctuation in gas turbine combustor *NASA CR* 212540

[5] Buttsworth D R and Jones T V 1998 A fast response total temperature probe for unsteady compressible flows *ASME J. Eng. Gas Turbines Power* **120** 601–7

[6] Chana K S 2004 Requirements for instrumentation technology for gas turbine propulsion systems—gas total surface temperature measurements for harsh environments *Advanced Measurement Techniques for Aeroengines and Stationary Gas Turbines* VKI LS 2004-04

[7] Gossweiler C, Kupferschmied P and Gyarmathy G 1995 On fast-response probes: I. Technology, calibration and application to turbomachinery *ASME J. Turbomach.* **117** 611–7

[8] Kupferschmied P, Köppel P, Gizzi W, Roduner C and Gyarmathy G 2000 Time-resolved flow measurements with fast-response aerodynamic probes in turbomachinery *Meas. Sci. Technol.* **11** 1036–54

[9] Pfau A, Schlienger J, Kalfas A I and Abhari R S 2003 3-dimensional flow measurement using a miniature virtual 4 sensors fast response aerodynamic probe (FRAP®) *ASME Paper* GT2003-38128

[10] Schlienger J P 2003 Evolution of unsteady secondary flows in a multistage shrouded axial turbine *Dissertation* ETH **No 15230**

[11] Kemp N H, Rose P H and Dedra R W 1959 Laminar heat transfer around blunt bodies in dissociated air *J. Aero/Space Sci.* **26** 421–30

[12] Schmidt E and Werner K 1941 Wärmeabgabe über den Umfang eines Angeblasenen Geheizten Zylinders *Forsch. Ing.-Wes.* **12** 65–73

[13] Schultz D L and Jones T V 1973 Heat transfer measurements in short duration facility hypersonic facilities *Agardograph* **165** 1–63

[14] Oldfield M L G, Burd H J and Doe N G 1982 Design of wide bandwidth analogue circuits for heat transfer instrumentation in transient wind tunnels *16th Symp. Int. Center for Heat and Mass Transfer* (New York: Hemisphere) pp 233–57

[15] Kupferschmied P 1998 Zur Methodik zeitaufgelöstter Messungen mit Strömungssonden in Verdichtern und Turbinen *Dissertation* ETH **No 12474**

[16] Prandlt L, Oswattisch K and Wieghardt K 1984 *Führer durch die Strömungslehre* (Braunschweig: Vieweg)

[17] Hunziker R and Gyarmathy G 1993 The operational stability of a centrifugal compressor and its dependence on the characteristics of the subcomponents *ASME Paper* 93-GT-284

[18] Bernsdorf S, Rose M and Abhari R S 2006 Modeling of film cooling: I. Experimental study of flow structure *ASME J. Turbomach.* **128** 141–9

[19] Schleer M W 2006 Flow structure and stability of a turbocharger centrifugal compressor *Dissertation* ETH **No 16605**

[20] Schleer M, Mokulys T and Abhari R S 2003 Design of a high pressure-ratio centrifugal compressor for studying Reynolds number effects *Int. Conf. Compressors and their Systems (London)* pp 391–404

[21] Mansour M, Chokani N, Kalfas A I and Abhari R S 2007 Unsteady entropy measurements in a high-speed radial compressor *ASME J. Eng. Gas Turbines Power* **130** 021603

[22] Burdet A and Abhari R S 2007 Influence of near hole pressure fluctuation on the thermal protection of a film-cooled flat plate *ASME Paper* HT2007-321812 (*ASME J. Heat Transfer* to be published)

[23] Mansour M, Aga V, Chokani N and Abhari R S 2008 Aerothermal aspects of a pulsated inclined film cooling jet in crossflow *AIAA Paper* 2008-4298

[24] Behr T, Kalfas A I and Abhari R S 2007 Unsteady flow physics and performance of a one-and-1/2-stage unshrouded high work turbine *ASME J. Turbomach.* **129** 348–59

[25] Mansour M, Chokani N, Kalfas A I and Abhari R S 2008 Impact of time-resolved entropy measurement on a one-and-1/2-stage axial turbine performance *ASME Paper* **GT2008-50807**